European Rotorcraft Forum

NUMERICAL INVESTIGATION OF BOUNDARY LAYER SEPARATION OVER AN AIRFOIL DURING DYNAMIC STALL

Sang Eon Jeon[1], Soo Hyung Park[2*], Yung Hwan Byun[3], Kai Richter[4] and Wolfgang Geissler[5]

[1]E-mail: eonman@korea.com, [2*]E-mail: pish@konkuk.ac.kr, Corresponding Author, [3]E-mail: yhbyun@konkuk.ac.kr, [4]E-mail: kai.richter@dlr.de, [5]E-mail: wolfgang.geissler@dlr.de

[1,2,3]Department of Aerospace Information Engineering, Konkuk University, Seoul, South Korea
[4,5]Institute of Aerodynamics and Flow Technology, DLR, Goettingen, Germany

Abstract

Boundary-layer separations appearing on an oscillating airfoil are investigated to understand the onset process of dynamic stall phenomena. Dynamic stall predictions are performed using a time-accurate Navier-Stokes solver coupled with the transition-transport equations of Langtry and Menter. The effects of the reduced frequency and the Mach number on the generation of separation bubbles are compared based on a parametric study. Four types of boundary-layer separations are observed over the OA209 airfoil: the laminar separation bubble, shock-induced separation, trailing edge separation, and an unsteady separation related to the dynamic stall vortex. Numerical results show that the appearance of the dynamic stall vortex is not directly related to the existence of the leading edge separations. The presence of the dynamic stall vortex and the resulting lift overshoot are strongly correlated with the reduced frequency of the oscillation.

1. INTRODUCTION

Dynamic stall has been considered as an unsteady phenomenon occurring on an airfoil under rapid pitching motion [1-5]. The dynamic stall over helicopter rotor blades seriously limits the high-speed and maneuvering flight capabilities of the helicopter. Strong unsteady fluctuations during dynamic stall often result in high vibration or stall flutter in forward flight. For over five decades numerous researches on the dynamic stall phenomena have been conducted based on experimental data [1-8]. Analytical [9,10] and numerical studies [11-14] have also been performed to understand the physics of dynamic stall.

The dynamic stall process has been categorized into two types: 'light' dynamic stall and 'deep' dynamic stall [2,3]. Light dynamic stall occurs at an angle of attack around the static-stall angle, where the dynamic pitching moment does not exceed the maximum value occurring during static stall. The onset of the dynamic stall process has been found to be sensitive to both the flow conditions and the pitching motion of the airfoil. Deep dynamic stall is characterized by a delayed massive separation. A lift overshoot past the static stall limit accompanies a large increase in the nose-down pitching moment. The delayed separation is generally explained by the formation and convection of the dynamic stall vortex (DSV) originating from the leading edge.

The onset of the dynamic stall process is associated with the generation of boundary-layer separations and their complex interaction due to the unsteady motion. According to the Reynolds number and the shape of the airfoil leading edge, there are different stall mechanisms: leading-edge stall and trailing-edge stall. Previous experiments [2,3,7,8] showed that at a low Mach number, a majority of airfoils experience trailing-edge-type dynamic stall, similar to the characteristics of static stall. A strong adverse pressure gradient on the upper surface results in trailing-edge separation (TES) at a high angle of attack. As the Mach number increases, leading-edge stall is likely to occur. The burst of the laminar separation bubble (LSB) is one of the major reasons behind the leading-edge stall at low Mach numbers [5,12]. A laminar separation bubble is often generated over the upper surface, even at low angles of attack and as the Reynolds number increases, the extent of the bubble region decreases. The LSB is strongly related to the separation-induced transition which causes the separated laminar boundary layer to reattach to the airfoil surface.

It is well known that the compressibility effect is very important when seeking to understand the dynamic stall onset [3,13]. Fukushima and Dadone [6-8] found that shock-induced separation (SIS) due to the formation of shock waves limits the rise of velocity suction in the leading edge of the airfoil. They stated that unsteady effects no longer cause any delay in the stall. McCroskey et al. [3] noted that

the onset of a supercritical flow corresponds to the conditions for which most airfoils began to show a decrease in the dynamic maximum lift coefficient with an increasing Mach number. It was also noted that the growth in the maximum local Mach number above sonic conditions caused a strong tendency toward leading-edge stall on all of the considered airfoils, regardless of their behavior at the low-Mach-number regime.

The above-mentioned dynamic stall phenomena, especially flow separations, are well discussed in recent papers [5,15-18], reflecting modern experimental and numerical techniques. Geissler and Trenker [16] explained that the creation of the dynamic stall vortex results from 'vorticity accumulation' in the leading edge and that the generation and the rapid ejection of the vorticity are closely related to the laminar separation and supersonic bubbles. Mulleners and Raffel [17] claimed from their PIV measurements that the onset of dynamic stall is strongly associated with shear layer instability and the resulting vortex-induced separation.

A laminar separation bubble (LSB), shock-induced separation (SIS) and trailing-edge separation (TES) are usually observed during the pitching motion. However the complex interactions between flow separations during the dynamic stall process are not well explained. In the present numerical study, the effects of the Mach number and reduced frequency on the dynamic stall onset are investigated to identify unsteady interactions between boundary-layer separations.

2. NUMERICAL METHOD

Parallelized compressible structured Navier-Stokes equations [19,20] and the shear stress transport (SST) $k-\omega$ turbulence model [21] combined with Langtry and Menter's transition-transport equations [22,23] were applied to the present numerical investigation.

Reynolds-averaged Navier-Stokes equations and $k-\omega$ Shear Stress Transport (SST) turbulence equations are used as the baseline governing equations [19]. The $\gamma - Re_\theta$ transition model of Menter et al. [21,22] is applied to dynamic stall flows in order to account for the laminar-turbulent transition phenomenon. The model consists of two transport equations for the intermittency, γ, and the transition momentum thickness Reynolds number, $\widetilde{Re}_{\theta t}$:

(1) $$\frac{\partial(\rho\gamma)}{\partial t}+\frac{\partial\left(\rho u_j\gamma\right)}{\partial x_j}=P_\gamma-E_\gamma+\frac{\partial}{\partial x_j}\left[\left(\mu+\mu_T\right)\frac{\partial\gamma}{\partial x_j}\right]$$

(2) $$\frac{\partial\left(\rho\,\tilde{\mathrm{Re}}_{\theta,t}\right)}{\partial t}+\frac{\partial\left(\rho u_j\,\tilde{\mathrm{Re}}_{\theta,t}\right)}{\partial x_j}=P_{\theta,t}+\frac{\partial}{\partial x_j}\left[2\left(\mu+\mu_T\right)\frac{\partial\,\tilde{\mathrm{Re}}_{\theta,t}}{\partial x_j}\right]$$

The production and destruction/relaminarization sources of intermittency in Eq. (1) are defined as follows:

(3) $$P_\gamma=F_{length}c_{a1}\rho S\left[\gamma F_{onset}\right]^{0.5}\left(1-\gamma\right)$$

(4) $$E_\gamma=c_{a2}\rho\Omega\gamma F_{turb}\left(c_{e2}\gamma-1\right)$$

Here, S is the strain-rate magnitude and Ω is the vorticity magnitude. The constants for the intermittency equation are $c_{a1}=2.0$, $c_{a2}=0.06$, and $c_{e2}=50$. F_{length} and F_{onset} are empirical correlations that control the length and onset location of transition region. F_{onset} is designed to trigger the intermittency production and to switch from zero in a laminar boundary layer to one downstream of the transition onset point. The correlations are formulated as functions of the local strain-rate Reynolds number, $Re_V=\rho y_n^2 S/\mu$, and the turbulent Reynolds number, $Re_T=c_\mu\rho k/(\mu\omega)$.

The intermittency transport equations govern the production and the destruction of the intermittency, which can control both the boundary layer transition and the relaminarization of an accelerated boundary layer. The transition onset criterion depends on the transition momentum thickness Reynolds number that can be determined by the second equation for $\widetilde{Re}_{\theta t}$. The transition onset Reynolds number is indeed a nonlocal function of the freestream turbulence intensity and streamwise pressure gradient. Some empirical correlations can be established to allow the nonlocal values outside the boundary layer to diffuse into the boundary layer. The transport equations for $\widetilde{Re}_{\theta t}$ are then composed of the source term for the transported scalar to match the local value of $Re_{\theta t}$ from an empirical correlation. This localization of the transition model has greatly improved the flexibility of CFD tools for engineering purposes.

The eddy viscosity μ_t is determined by the following formulation:

(5) $$\mu_T=\min\left[c_\mu\frac{\rho k}{\omega};\frac{0.31\rho k}{SF_2}\right]$$

Here, F_2 is a blending function that is designed to be 1 for boundary-layer flows and 0 for free shear layers. The effective intermittency is obtained from

(6) $$\gamma_{sep}=\min\left(s_1\max\left[0,\left(\frac{\mathrm{Re}_V}{3.235\,\mathrm{Re}_{\theta c}}\right)-1\right]F_{reattach},2.0\right)F_{\theta t}$$

(7) $$F_{reattach}=e^{-\left(\frac{R_T}{20}\right)^4}$$

$$\gamma_{eff}=\max(\gamma,\gamma_{sep})$$

where γ_{sep} is the modified intermittency to correct the intermittency growth rate in the separation region. To prevent the laminar separation from becoming too long, this modification allows the local

intermittency to exceed 1.0 where the laminar boundary layer separates. The constant s_1 controls the size of the separation bubble, which is set to 3.0 from the numerical experiments in the present study. The effective intermittency is applied only to the k equation, but the original form of the ω equation is always retained. The effective intermittency in the destruction term of the k equation should be bounded from a small value to 1.0 to avoid unphysical growth of the turbulent kinetic energy in the laminar boundary layer:

$$\tilde{\gamma}_{eff} = \min(\max(\gamma_{eff}, 0.1), 1.0) \quad (8)$$

The value of k is set to zero at the wall while ω is specified as an asymptotic value, $(60\mu_L) / (c_\mu \rho d^2)$, where d is the distance of the first cell center from the wall. Boundary conditions for both γ and $\widetilde{Re}_{\theta t}$ are zero normal fluxes at the wall. In a freestream condition, γ_∞ is equal to 1.0, while $\gamma - \widetilde{Re}_{\theta t}$ is calculated from the empirical formulation of transition-onset Reynolds number with zero pressure gradient. These boundary conditions are permitted for the turbulent freestream condition, as the present transition model can be applied to a bypass transition subjected to freestream turbulence. The freestream turbulence is controlled by the turbulent intensity and the freestream eddy viscosity.

The governing equations in the physical coordinate system are transformed into computational coordinates and are discretized by a cell-centered finite volume method. The inviscid flux requires artificial dissipation to prevent numerical instability. Roe flux-difference splitting and the third-order MUSCL are used with the Van-Albada limiter to obtain second-order accuracy. For a low subsonic flow, the third-order or fifth-order MUSCL without a limiter can be applied for all solution variables without any difficulties in stability. A simple central differencing scheme is employed to obtain the variable gradients of the viscous fluxes. It should be noted that second- or higher-order discretization for both turbulence and $\gamma - \widetilde{Re}_{\theta t}$ equations greatly improves the accuracy of transition prediction [19].

A dual-time stepping technique was employed for the second-order time-accurate simulations [20]. The second-order backward differencing method is used to advance the solution in physical time. The diagonalized alternating-direction implicit (DADI) method is applied for pseudo-time stepping to find steady-state solutions at each physical time. A loosely coupled algorithm is used to integrate the Navier-Stokes, $k - \omega$ and $\gamma - \widetilde{Re}_{\theta t}$ equations separately. The source vectors of the turbulence and transition equations should be treated implicitly because they result in a stiffness problem in the DADI method. The contributions of the dissipation terms in each equation are added in the implicit parts to increase diagonal dominance. Numerical details and special treatments for convergence enhancement can be found in the literature [19,20].

3. NUMERICAL RESULTS

A C-type airfoil grid system was used with 512 and 120 cells in the streamwise and wall-normal directions, respectively. Far-field boundaries were located 40 chord lengths away from the quarter chord position of the OA209 airfoil [24,25]. The cell spacing for the first grid point from the wall boundary is $2.5 \times 10^{-6} c$ (chord length), which is sufficient to resolve the viscous sublayer in the turbulent boundary layer. Leading-edge separations (laminar separation bubble and shock-induced separation) typically have very small sizes and weak strength at high Reynolds numbers. As shown in Fig.1, sufficient grid points and orthogonality of high quality were required to achieve the present research purpose. About 2,000 time steps per cycle and 500 pseudo-time sub-iterations at each physical time step were used, confirmed by a parameter refinement study including grid refinement. Approximately 800 time steps at least are usually required for the temporal convergence of the main stall event [14].

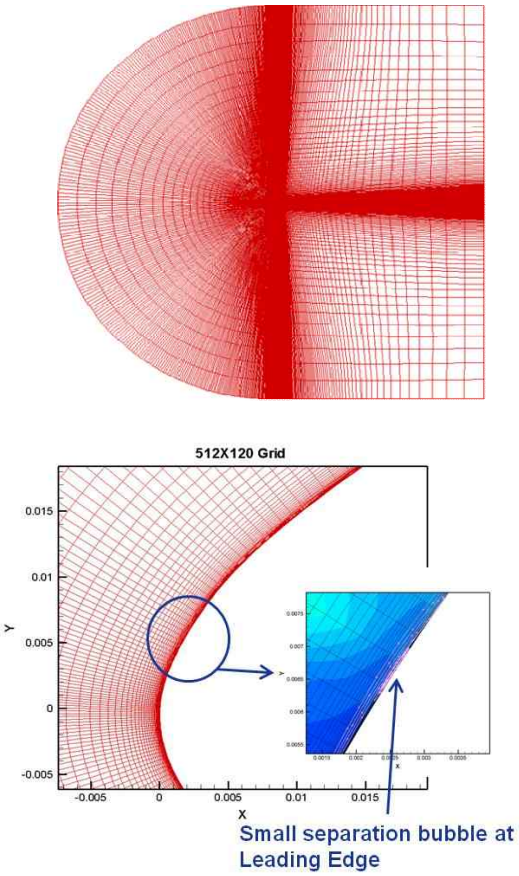

Fig. 1. OA209 airfoil grid: (left) full geometry, (right) close view around the leading edge.

Sinusoidal pitching oscillation for the angle of attack, $a(t) = 9.8 + 10.3\sin(2kt^*)$, was enforced on the OA209 airfoil. Computational results for the reduced frequency, $k = 0.025$, and the Mach number, $M = 0.3085$, were compared with experimental data [25] as a validation case. Figure 2 displays the lift coefficient variations with the angle of attack at the reduced frequency of 0.025 for the fully turbulent $k-\omega$ SST model and the present transition transport model. The fully turbulent computation predicted a higher lift peak at an earlier angle of attack compared to the experimental data. Using the transition transport model the lift overshoot due to the dynamic stall vortex was predicted better and the strength of the lift peak was considerably reduced. This means that accurate, i.e. highly sophisticated transition prediction is necessary to investigate the development of the dynamic stall vortex. The present transition model enables us to predict transition to turbulence via a laminar separation bubble. Figure 3 illustrates the skin friction distribution during the dynamic stall process with an angle of attack from 15.3 to 17.6 degrees. Blue-colored regions denote the negative skin friction where separation exists. At the initial stage of the dynamic stall process, a laminar separation bubble (LSB) on the upper surface is observed. Indeed, the bubble is already generated at small to moderate angles of attack, leading to very thin and long stretched bubble-shapes. When increasing the angle of attack, the bubble moves forward and the length of the bubble shrinks. Trailing edge separation (TES) also occurs prior to the dynamic stall event. The TES moves forward as the angle of attack is increased.

Figure 4 shows instantaneous vorticity and skin friction distributions at 15.75 and 15.88 deg incidences. Positive vorticity means that the flow rotates clockwise and a separation exists on the surface. It is clear that a particular 'isolated' separation abruptly emerges at about 30 % chord position. The positive vorticity becomes stronger and it merges with that from the TES, as the angle of attack is increased to 15.88 degree incidence. At this incidence the TES is fully merged with the particular separation, as shown in Fig. 4(b). This new type of separation, which could not be found in the steady computations, is independent of the LSB and TES. In this paper the new type of separation is denoted as "dynamic stall separation" (DSS).

Figure 5 displays the vorticity distribution and streamlines at 15.88 deg incidence, just at the moment of the merging event between the TES and DSS. The figure clearly shows that the dynamic stall vortex (DSV) begins to emerge from the dynamic stall separation (DSS). It turns out that this separation is resulted from the strong shear layer, which is accumulated and ejected from the leading edge. The shear layer exists even in steady cases at high angles of attack. However, the shape of the unsteady shear layer is distorted due to the unsteady pitching motion. The positive vorticity at about 30 % chord position is transferred from the distortion of the shear layer. It should be noted that the LSB, TES, and the supersonic bubbles were found even in the steady computation with given the same airfoil and flow conditions. The DSV, which is purely unsteady, creates the lift overshoot and its shedding causes the following fluctuation of the aerodynamic loads.

Figure 6 illustrates the pressure coefficient distributions with angle of attack. A supersonic bubble is developed at the leading edge of the airfoil and becomes attenuated as the angle of attack is increased, as shown in Fig. 6. It was also observed that at higher reduced frequencies the maximum local Mach number at the leading edge is reduced because the relative flow velocity is decreased due to the faster pitch-up motion. Figure 7 shows Mach contours at 14.1 deg incidence. Weak shock waves are embedded above the laminar separation bubble and the laminar boundary layer becomes a thicker turbulent boundary layer after the turbulent transition. Figure 8 compares the skin friction distributions near the leading edge between results of fully turbulent and transitional flows. At this angle of attack laminar separation was already generated in the vicinity of the supersonic flow prior to the onset of the supersonic bubble. The adverse pressure gradient due to shock waves locally decelerates the flow velocity and is likely to trigger transition to turbulence. This adverse effect also exists in the fully turbulent flow and causes a very small separation bubble, which is termed a shock-induced separation bubble (SISB). It can be inferred that the SISB is a different phenomenon compared to the laminar separation bubble, but its effect on the dynamic stall process is quite similar.

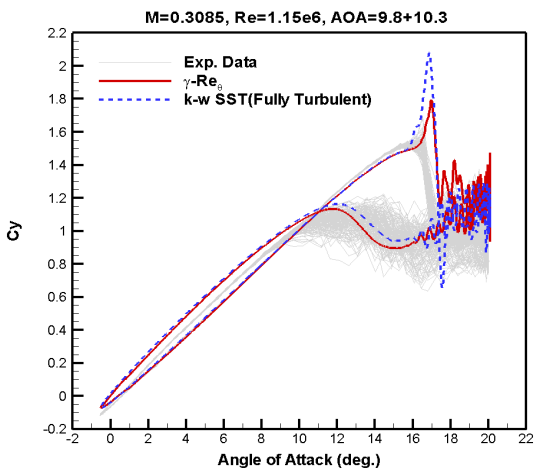

Fig. 2. Effect of the transition model on the development of a dynamic stall vortex for the baseline case

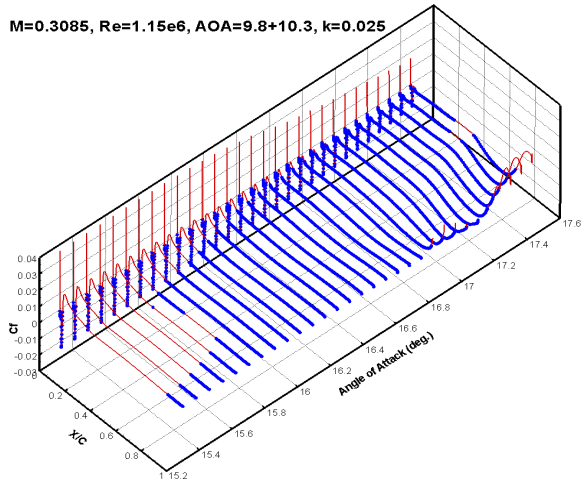

Fig. 3. Time history of skin friction coefficient for the baseline case: (blue) negative skin friction

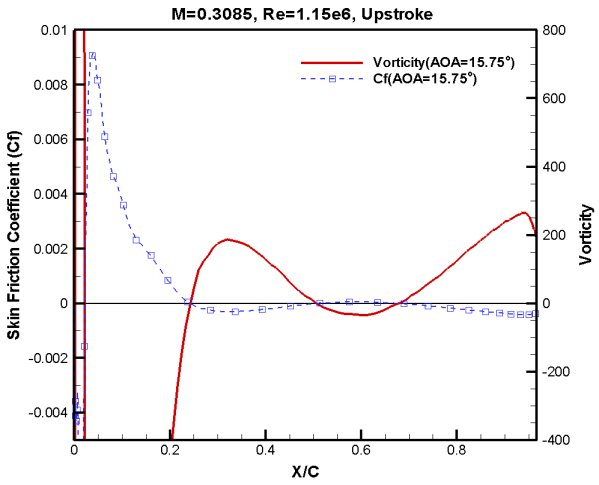

(a)

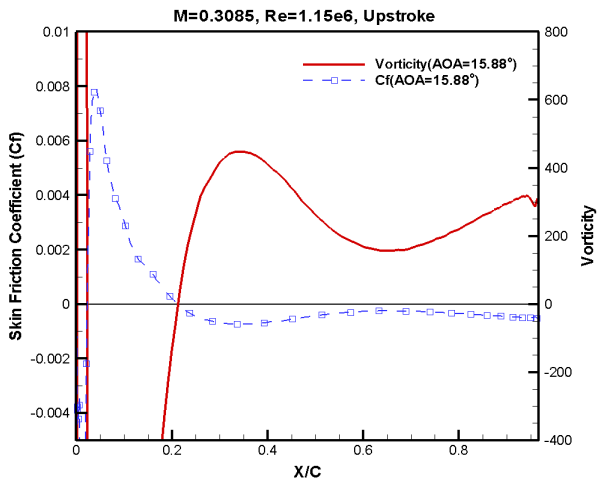

(b)

Fig. 4. Instantaneous surface vorticity and skin friction coefficients, (a) α=15.75, (b) α=15.88 degrees

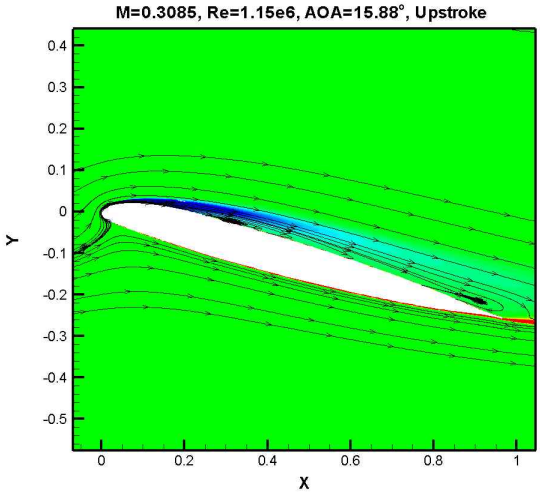

Fig. 5. Instantaneous vorticity and streamline contours (α=15.88 deg.)

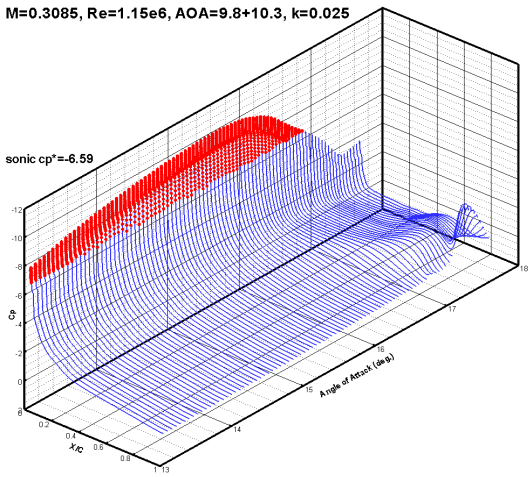

Fig. 6. Time history of the pressure coefficient for the baseline case: (red) supersonic region

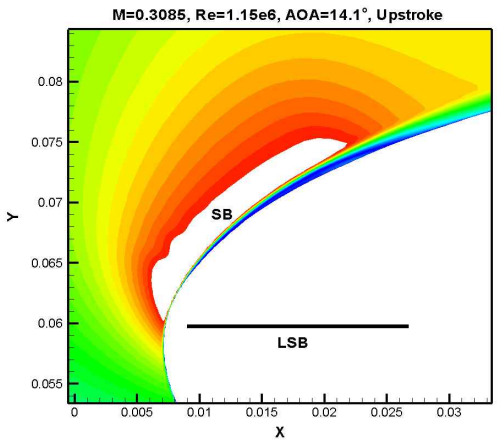

Fig. 7. Mach contours and supersonic bubble at the leading edge: (white) supersonic region, AOA=14.1 deg.

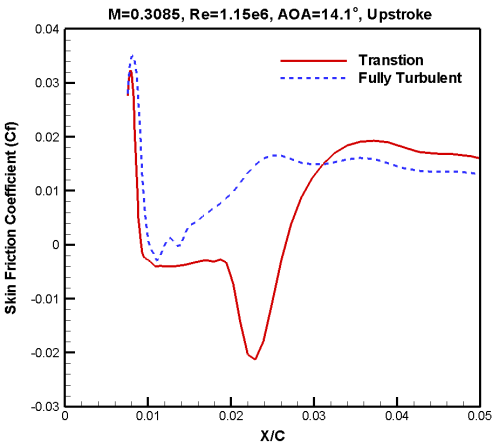

Fig. 8. Comparison of skin friction coefficient for the baseline case

A parametric study at different Mach numbers (M=0.2, 0.3, and 0.4) and reduced frequencies (k=0.0125, 0.025, and 0.05) was conducted to understand the effects of the two key parameters on the dynamic stall phenomena. Figure 9 displays a comparison of the lift coefficients with reduced frequencies at each Mach number. At a reduced frequency of 0.0125, lift overshoot was not observed during dynamic stall. A careful investigation in the present work proves that there is no lift overshoot when the dynamic stall vortex is not observed. According to the Mach number, either trailing edge separation (TES) or leading edge separations (LSB and SISB) can initiate the dynamic stall onset. For low Mach numbers, the trailing edge separation is responsible for the onset of dynamic stall. As the reduced frequency increases at a fixed Mach number, the lift overshoot becomes stronger and the dynamic stall is delayed. It was also observed that the maximum local Mach number at the leading edge is reduced because the relative flow velocity is decreased due to a faster pitch-up motion. This means that a higher reduced frequency produces a similar effect on the leading-edge phenomena as a lower Mach number.

Figure 10 displays the onset angles of the trailing-edge separation and the leading edge separation bubble during the upstroke motion. As the Mach number increases, the onset angles are decreased at a fixed reduced frequency. The LSB is formed at a small angle of attack, whereas the onset angle of the TES is well correlated with the angle at which the slope of the lift coefficient begins to degrade. Figure 11 shows the maximum lift coefficients and the corresponding angles of attack. As the Mach number increases, the angle of attack at the maximum lift coefficient is decreased, whereas the maximum lift coefficient itself decreases by much less. The maximum value of the lift coefficient is associated with the reduced frequency; Increased reduced frequency corresponds to increased maximum lift coefficients. It can be inferred that the lift overshoot due to the appearance of the dynamic stall vortex is closely related to the unsteady pitching velocity that is linked to the speed of the vortex shedding.

Table 1 summarizes the separation bubbles appearing over the airfoil surface for all cases investigated. At low Mach numbers, trailing edge separation opens the stall process for the OA209 airfoil, while the appearance of the dynamic stall vortex depends on the reduced frequency. No dynamic stall vortices and resulting lift overshoot were found in the low-reduced-frequency cases. Shock-induced separation occurred at both M=0.3 and 0.4. The laminar separation bubble did no longer appear if the Mach number exceeded 0.4 (not presented here). The existence of leading-edge separation may be independent of the reduced frequency, although unsteady effects change their locations and sizes. The leading-edge separations appear to initiate at the onset of the dynamic stall vortex for some cases because they can produce large amounts of spanwise vorticity in the boundary layer [4,16]. On the other hand, it is quite clear that the appearance of the dynamic stall vortex does not have a direct relationship with the existence of the leading edge separations.

The dynamic stall separation in the middle of the airfoil, as found in the present investigation, is thought to have resulted from the vortex roll-up process of the strong shear layer developing from the leading edge of the airfoil [17]. The stall separation is quickly merged with the trailing edge separation for the deep dynamic stall cases, whereas no stall separation appeared at low reduced frequencies in the light dynamic stall cases. Although the present investigation is limited to RANS computations and further study is essential, the present numerical results imply that the Kelvin-Helmholtz instability and the consequent vortex roll-up of the shear layer is the direct cause of the dynamic stall vortex.

Table 1. Separation bubbles on the upper surface of the OA209 airfoil during the dynamic stall process

	k=0.0125	k=0.025	k=0.05
M=0.2	LSB TES	LSB TES DSV	LSB TES DSV
M=0.31 And M=0.4	LSB SISB TES	LSB SISB TES DSV	LSB SISB TES DSV

* LSB: laminar separation bubble, TES: trailing edge separation, SISB: shock-induced separation bubble, DSV: dynamic stall vortex

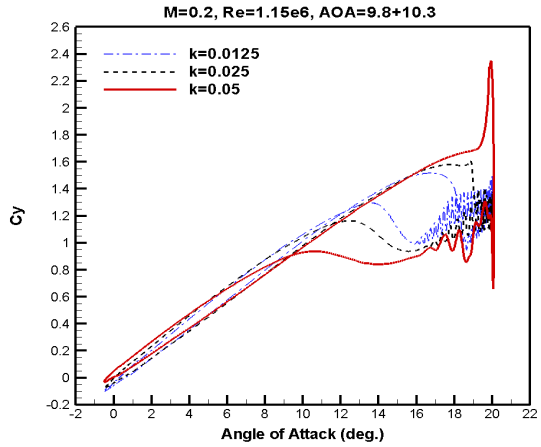

(a)

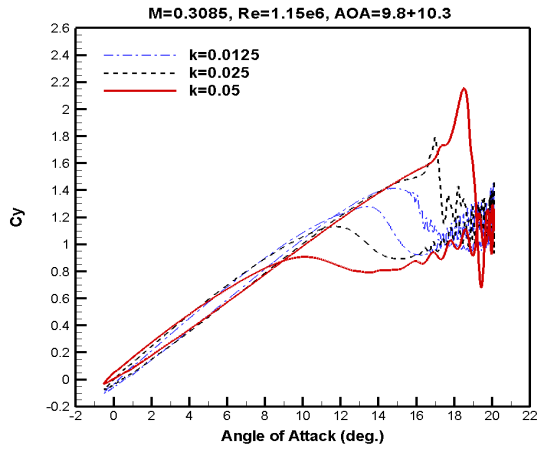

(b)

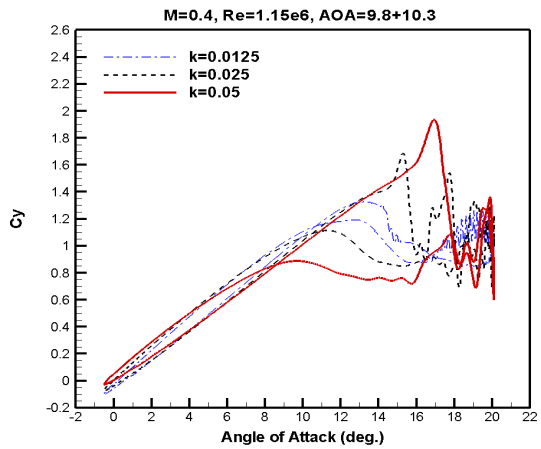

(c)

Fig. 9. Lift coefficient variation with reduced frequency at (a) M=0.2, (b) 0.31, and (c) 0.4

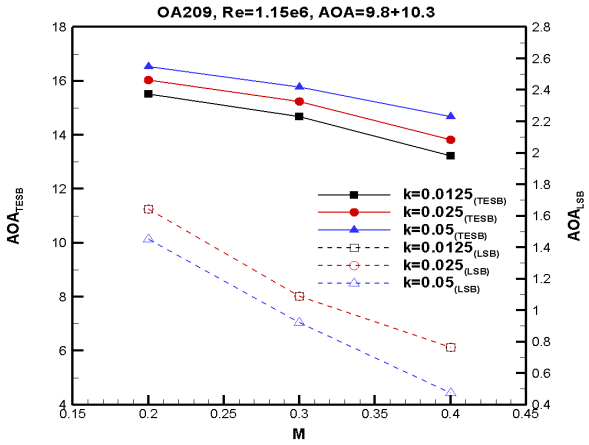

Fig. 10. Onset angles of attack with reduced frequency at M=0.2, 0.31, and 0.4: (left axis) for the trailing edge separation, and (right axis) for the laminar separation

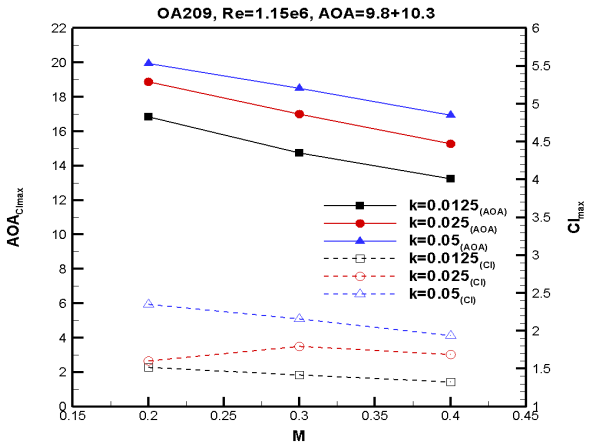

Fig. 11. Angle of attack and maximum lift coefficient with reduced frequency at M=0.2, 0.31, and 0.4: (left axis) angle of attack at the max. lift coefficient, (right axis).

4. CONCLUDING REMARKS

Unsteady compressible RANS computations were performed to investigate boundary-layer separations during the dynamic stall process. In order to take into account the turbulent transition, the transition transport equations were coupled with the $k-\omega$ turbulence model. Numerical results showed that the transition prediction provides closer agreement of the lift coefficient with experimental data for the baseline case dynamic stall investigations.

The effects of Mach number and reduced frequency, as the two key parameters, were investigated for dynamic stall flows over the OA209 airfoil. Four types of boundary-layer separation were found over

the OA209 airfoil: laminar separation bubble, shock-induced separation, trailing edge separation, and an unsteady separation called “dynamic stall separation” specifically relating to the onset of the dynamic stall vortex. As the Mach number increases, the onset angles of leading-edge separations are decreased at a fixed reduced frequency.

At low Mach numbers trailing edge separation opens the stall process for the OA209 airfoil, while the appearance of the dynamic stall vortex depends on the reduced frequency. Dynamic stall vortices and the resulting lift overshoot were not found in cases involving low reduced frequencies. The appearance of the dynamic stall vortex is not directly related to the existence of the leading edge separations, though leading edge separations can initiate the onset of the dynamic stall vortex.

ACKNOWLEDGEMENT

This research was supported by the EDISON Program through the National Research Foundation of Korea (NRF) funded by the Ministry of Education, Science and Technology (2011-0020560).

REFERENCES

[1] McCroskey, W.J., “The Phenomenon of Dynamic Stall,” NASA TM81264, 1981.

[2] McCroskey, W. J., “Unsteady Airfoils,” Annual Review of Fluid Mechanics, Vol. 14, pp.285-311, 1982.

[3] McCroskey, W. J., McAlister, K. W., Carr, L. W., Pucci, S. L., Lambert, O., and Indergand, R. F., “Dynamic Stall on Advanced Airfoil Sections,” AHS Journal, Vol. 26, No.7, pp.4-50, 1981.

[4] Carr, L. W., “Progress in Analysis and Prediction of Dynamics Stall,” Journal of Aircraft, Vol.25, No.1, pp.6-17, 1988.

[5] Carr, L. W., and Chandrasekhara, M. S., “Compressibility Effects on Dynamic Stall,” Progress in Aerospace Sciences, Vol. 32, pp. 523-573, 1996.

[6] Fukushima, T. and Dadone, L. U., “Comparison of Dynamic Stall Phenomena for Pitching and Vertical Translation Motions,” NACA CR-2793, 1976.

[7] McAlister, K. W., Carr L. W., and McCroskey, W. J., “Dynamic Stall Experiments on the NACA0012 Airfoil,” NASA TP-1100, 1978.

[8] Katary, M., “An Experimental Study of the Development of a Supersonic Zone near the Leading Edge of an Airfoil Oscillating in Subsonic Flow,” AIAA Paper 83-2133, 1983.

[9] Leishman, J., and Beddoes, T., “A Semi-Empirical Model for Dynamic Stall,” Journal of AHS, Vol.34, No.3, pp.3–17, 1989.

[10] Sheng, W., Galbraith, R. M., Coton, F., “A New Stall-Onset Criterion for Low Speed Dynamic Stall,” Journal of Solar Energy Engineering, Vol.128, pp.461–471, 2006.

[11] Visbal, M. R., “Dynamic stall of a constant-rate pitching airfoil,” Journal of Aircraft, Vol. 27, No.5, pp.400-407, 1990.

[12] Ekaterinaris, J. A., Srinivasan, G. R. and McCroskey, W. J., “Present capabilities of predicting two dimensional dynamic stall,” AGARD CP-522, Paper No. 1, 1994.

[13] Geissler, W., and Haselmeyer, H., “Investigation of dynamic stall onset,” Aerospace Science and Technology, Vol. pp590-600, 2006.

[14] Richter, K., Le Pape, A., Knopp, T., Costes, M., Gleize, V., and Gardner, A.D., “Improved Two-Dimensional Dynamic Stall Prediction with Structured and Hybrid Numerical Methods” AHS Journal, Vol. 56, No. 4, 2011.

[15] Choudhuri, P. G., and Knight, D., “Effects of compressibility, pitch rate, and Reynolds number on unsteady incipient boundary layer separation over a pitching airfoil,” AIAA Paper 95-0782, 1995.

[16] Geissler, W., and Trenker, “Numerical Investigation of Dynamic Stall Control by a Nose-Drooping Device,” AHS-Specialist Meeting, San Francisco, CA, Jan. 2002.

[17] Mulleners, K., and Raffel, M., “The Onset of Dynamic Stall Revisited,” Experiments in Fluids, 24 May 2011.

[18] Bowles, P. O., Coleman, D. G., Corke, T. C., and Thomas, F. O., “Compressibility Effects on Aerodynamic Damping during Dynamic Stall Events,” AHS 68th Annual Forum, Fort Worth, Texas, May 2012.

[19] Park, S.H., and Kwon, J.H., "Implementation of Turbulence Models in an Implicit Multigrid Method," AIAA journal, Vol.42, No.7, pp.1348-1357, 2004.

[20] Park, S.H., and Kwon, J.H., “Comparisons of Steady and Unsteady methods for Pitch-Damping Predictions,” AIAA 2003-3671, 21st AIAA Applied Aerodynamics Conference, Orlando, Florida, June 2003.

[21] Menter, F. R., “Two-Equation Eddy-Viscosity Turbulence Models for Engineering Applications,” AIAA Journal, Vol. 32, No.8, pp.1598-1605, 1994.

[22] Langtry, R., and Menter, F. R., “Correlation-

Based Transition Modeling for Unstructured Parallelized Computational Fluid Dynamics Codes," AIAA Journal, Vol. 47, No. 12, pp.2894-2906, 2009.

[23] Menter, F. R., Langtry, R., and Volker, S., "Transition Modeling for General Purpose CFD Codes," Flow Turbulence Combustion, Vol.77, pp.277-303, 2006.

[24] Thibert, J. J., and Gallot, J., "Advanced Research on Helicopter Blade Airfoils," *Vertica*, Vol. 5, No. 3, 1981, pp. 279–300.

[25] Geissler, W., Dietz, G., Mai, H., Bosbach, J., and Richard, H., "Dynamic Stall and its passive Control Investigations on the OA209 Airfoil Section," 31st-European Rotorcraft Forum, Florence, Italy, Sept. 2005.